



Compact and broad wavelength range tunable orbital angular momentum mode generator based on cascaded helical photonic crystal fibers

CAILING FU,^{1,2,3}  PENGFEI LI,^{1,2,3} ZHIYONG BAI,^{1,2,3}  SHEN LIU,^{1,2,3}  AND YIPING WANG^{1,2,3,4,*}

¹Guangdong and Hong Kong Joint Research Centre for Optical Fiber Sensors, College of Physics and Optoelectronic Engineering, Shenzhen University, Shenzhen 518060, China

²Guangdong Laboratory of Artificial Intelligence and Digital Economy (SZ), Shenzhen University, Shenzhen 518060, China

³Key Laboratory of Optoelectronic Devices and Systems of Ministry of Education and Guangdong Province, Shenzhen University, Shenzhen 518060, China

⁴Shenzhen Photonic Sensing Technology Co., Ltd, Shenzhen 518000, China

*Corresponding author: ypwang@szu.edu.cn

Received 8 June 2020; revised 26 July 2020; accepted 3 August 2020; posted 3 August 2020 (Doc. ID 399390); published 4 September 2020

A compact and broad wavelength range tunable orbital angular momentum (OAM) generator was experimentally demonstrated by cascading two helical photonic crystal fibers (HPCFs) with opposite helicity, i.e., clockwise-twisted + anticlockwise-twisted HPCF. Such an OAM generator exhibited a length of approximately 9 mm and generated a high-quality OAM mode with a wavelength range of 35 nm. Moreover, the wavelength range is expected to be tuned from 17.9–51.3 nm by applying mechanical torsion. © 2020 Optical Society of America

<https://doi.org/10.1364/OL.399390>

The orbital angular momentum (OAM) beam has gained great attention and exhibited various applications in optical communication [1], optical tweezer [2], and imaging [3]. Using OAM modes is an attractive way to achieve a higher transmission capacity in the mode-division multiplexing (MDM) communication system. Researchers have recently demonstrated various all-fiber OAM mode generators based on conventional long period fiber gratings (LPFGs) [4–6], helical fiber gratings (HFGs) [7–9], and fiber couplers [10,11]. For example, a few researchers have demonstrated OAM generators based on LPFGs in different types of fiber by means of CO₂ laser [4,6], mechanical microbend [5], and an acoustically induced technique [12]. The author also reported low-order and high-order OAM mode generators based on HFGs in a standard single mode fiber (SMF) [7], few-mode fiber (FMF) [8], and photonic crystal fiber (PCF) [9] by use of the hydrogen–oxygen flame heating technique. However, the aforementioned OAM modes could only be generated around the resonant wavelength, i.e., having a narrow wavelength range, which limited the development and application in the MDM communication system. Existing ways to generate OAM modes within a broad wavelength range are usually based on free-space methods, such as metamaterials [13], ultracompact silicon chip [14], and spiral

antenna array [15]. Recently, several all-fiber broad OAM mode generators were proposed and demonstrated, such as employing a fused or offset-spliced fiber coupler [16,17], LPFG based on dual-resonance coupling mechanism [18], and three-section length apodized phase-shifted LPFG [19]. Unfortunately, these fiber devices have to combine with external devices, e.g., rotator or polarization controller, to generate broad OAM modes, resulting in the complex systems. In addition, it is difficult to tune the wavelength range of these devices due to the fixed structure or grating pitch.

In this Letter, a compact and broad wavelength range tunable OAM generator was demonstrated by cascading two helical PCFs (HPCFs) with opposite helicity, i.e., clockwise-twisted (CT) + anticlockwise-twisted (ACT) HPCF. The effect of the resonant wavelength interval and cascaded helical direction on the transmission spectrum of the cascaded HPCFs, i.e., CT + ACT and ACT₁ + ACT₂ HPCF, was investigated to develop a broad OAM mode generator. Moreover, the beam profiles and interference patterns for the OAM modes generated by the cascaded CT + ACT and ACT₁ + ACT₂ HPCFs were demonstrated within a broad wavelength range. Furthermore, the wavelength range of the cascaded CT + ACT HPCFs could be tuned by applying mechanical torsion.

In our early work, we have achieved an inflated CT-HPCF and ACT-HPCF by use of an inflation-assisted hydrogen–oxygen flame heating technique. In our current work, the experimental setup and detailed operation procedures to fabricate the CT-HPCF and ACT-HPCF are exactly the same as the ones that are reported in Refs. [9,20], i.e., twisting the PCF with clockwise and anticlockwise directions via the rotating motor. First, each end of the CT-HPCF or ACT-HPCF was spliced to SMF to obtain the optimum resonant wavelength and coupling attenuation, as illustrated by the black or red curves in Figs. 2 and 3. Then, the end of SMF for two obtained HPCF samples was fused together by using a fusion splicer, as shown in Fig. 1. Consequently, two types of cascaded HPCFs with the

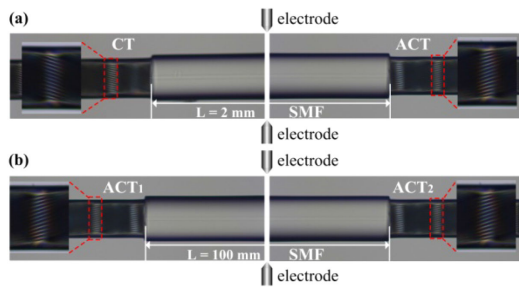


Fig. 1. Side-view microscope images of cascaded HPCFs with an (a) opposite helicity, i.e., CT + ACT HPCF, and (b) same helicity, i.e., ACT₁ + ACT₂ HPCF, where the distance, i.e., a total length of the middle SMF, between two HPCFs is 2 and 100 mm, respectively.

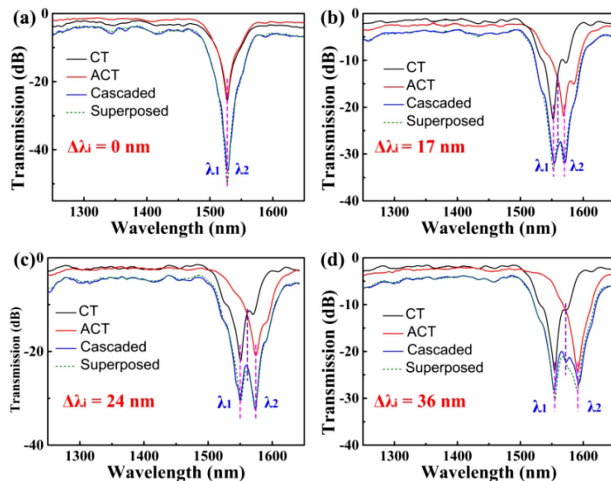


Fig. 2. Transmission spectra of four cascaded CT + ACT HPCFs with a resonant wavelength interval of (a) $\Delta\lambda_i = 0$, (b) $\Delta\lambda_i = 17$, (c) $\Delta\lambda_i = 24$, and (d) $\Delta\lambda_i = 36$ nm, respectively, where the black, red, blue, and dotted green curve represents the transmission spectrum of the CT-HPCF, ACT-HPCF, cascaded, and superposed HPCFs, respectively.

opposite or same helicities, i.e., CT + ACT and ACT₁ + ACT₂ HPCF, were obtained, where an opposite or same periodic pattern of the helical air holes were observed on the surface of the cascaded HPCFs, respectively. Two ends of the achieved cascaded HPCFs were spliced with the SMF to measure its transmission spectrum by use of a light source and an optical spectrum analyzer with a resolution of 0.2 nm.

To investigate the effect of the resonant wavelength interval on the transmission spectrum, four cascaded CT + ACT HPCF samples with different resonant wavelength intervals, i.e., $\Delta\lambda_i = 0, 17, 24, 36$ nm, were fabricated. Note that the resonant wavelength interval, i.e., $\Delta\lambda_i$, is given by the equation $\Delta\lambda_i = \lambda_2 - \lambda_1$, where λ_1 and λ_2 are the initial resonant wavelengths of two HPCF samples, respectively, as shown in Figs. 2 and 3. First, a CT-HPCF and ACT-HPCF with a coupling attenuation of -25.7 and -24.7 dB, respectively, at the same resonant wavelength, i.e., 1527.6 nm, as illustrated by the black and red curve in Fig. 2(a), were cascaded together. A resonance dip with an enhanced coupling attenuation of the -45.9 dB at the same resonant wavelength, i.e., 1527.8 nm,

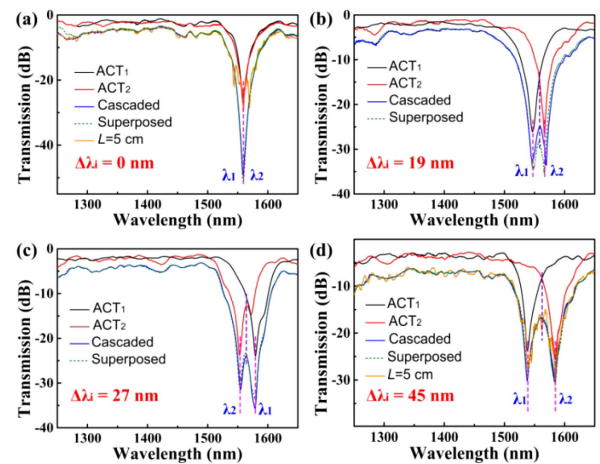


Fig. 3. Transmission spectra of four cascaded ACT₁ + ACT₂ HPCFs with a resonant wavelength interval of (a) $\Delta\lambda_i = 0$, (b) $\Delta\lambda_i = 19$, (c) $\Delta\lambda_i = 27$, (d) $\Delta\lambda_i = 45$ nm, respectively, where the black, red, blue, and dotted green curves represent the transmission spectrum of the ACT₁ - HPCF, ACT₂ - HPCF, cascaded, and superposed HPCFs, respectively. And the orange curve represents the interference spectrum when decreasing the total length of the middle SMF from 10 to 5 cm.

was exhibited, as illustrated by the blue curve in Fig. 2(a), indicating that the coupling attenuation could be strengthened by cascading two HPCFs with the same resonant wavelength. Then, a cascaded HPCF sample consisting of a CT-HPCF and ACT-HPCF with a resonant wavelength interval of 17 nm, i.e., $\Delta\lambda_i = 17$ nm, was fabricated, as shown in Fig. 2(b). As shown by the blue curve in Fig. 2(b), two resonance dips exist, where the resonant wavelengths correspond to the initial resonant wavelengths of the CT-HPCF and ACT-HPCF, i.e., 1552.0 and 1569.1 nm, respectively. And the central wavelength, i.e., 1562.9 nm, is the intersection of two transmission spectra, corresponding to a small peak in the transmission spectrum. The coupling attenuation was also increased from 22.0 to 32.0 dB. As shown in Figs. 2(c) and 2(d), the transmission spectra of the cascaded HPCFs with different resonant wavelength intervals, i.e., $\Delta\lambda_i = 24, 36$ nm, exhibited a similar trend with Fig. 2(b). Moreover, the obtained transmission spectrum of the cascaded HPCFs agreed well with the superposed HPCFs, i.e., mathematical addition of the transmission spectrum for the CT-HPCF and ACT-HPCF samples, as illustrated by the blue and green dotted curve in Fig. 2, also is in good agreement with the previously reported simulation with an additional oil region between two cascaded HFGs [21].

To investigate the effect of the cascaded helical direction on the transmission spectrum, four cascaded HPCF samples with the same helicity but different resonant wavelength intervals, i.e., $\Delta\lambda_i = 0, 19, 27, 45$ nm, were also fabricated. As shown in Fig. 3, the obtained transmission spectra of the cascaded ACT₁ + ACT₂ HPCFs are the same as the cascaded CT + ACT HPCFs in Fig. 2. Note that an obvious interference spectrum could be observed for cascaded ACT₁ + ACT₂ HPCFs when decreasing the distance, i.e., a total length of the middle SMF between two HPCF samples from 100 to 50 mm, attributed to the similar mechanism as the cascaded conventional LPFGs [22], as illustrated by the orange curves in Figs. 3(a) and 3(d), while the transmission spectrum of the cascaded CT + ACT

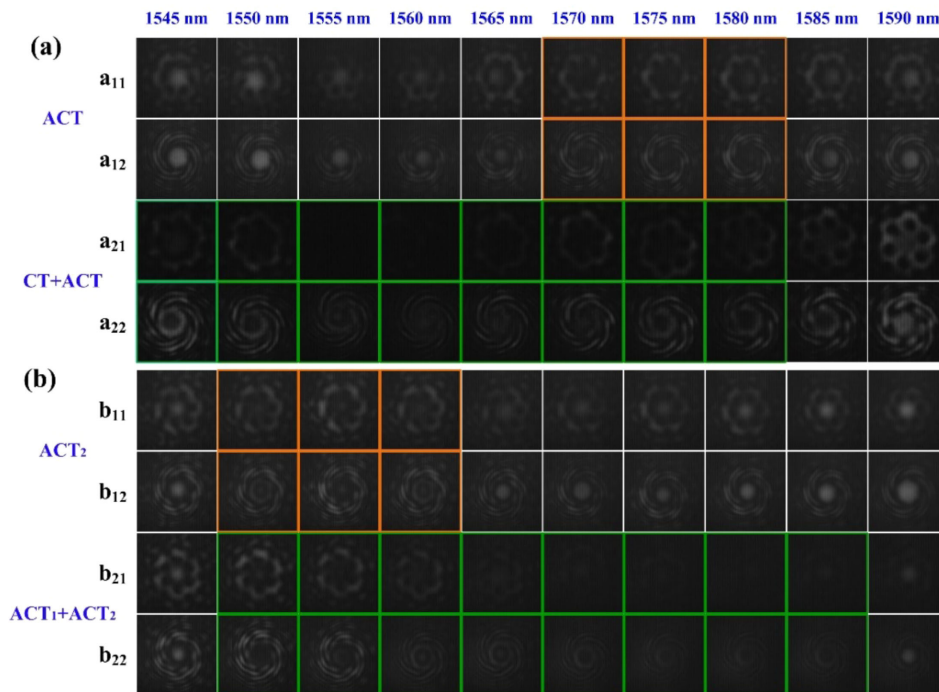


Fig. 4. Beam profiles and interference patterns for the OAM modes generated by (a) single ACT-HPCF, cascaded CT + ACT HPCFs and (b) single ACT₂ - HPCF, cascaded ACT₁ + ACT₂ HPCFs from 1545–1590 nm with a step of 5 nm, respectively. a_{i1} and b_{i1} illustrate the beam profiles; a_{i2} and b_{i2} illustrate the interference patterns, where $i = 1, 2$.

HPCFs was not affected by the distance. Thus, in this experiment the distance is 2 and 100 mm for the cascaded CT + ACT and ACT₁ + ACT₂ HPCF, respectively. This indicated that the transmission spectra of the cascaded HPCFs, i.e., CT + ACT and ACT₁ + ACT₂, could be regarded as the superposition of two individual HPCFs spectra when the distance between two HPCFs is appropriate, regardless of the cascaded helical direction. Compared with the cascaded ACT₁ + ACT₂ HPCFs, the CT + ACT HPCFs exhibited a compact size, i.e., a length of approximately 9 mm, as the optimum length of a single HPCF previously reported is 3.4 mm [9].

In our early work, a high-quality OAM₊₆ and OAM₋₆ mode could be generated by the CT-HPCF and ACT-HPCF at the resonant wavelength, respectively [20]. In our current work, the beam profile and interference pattern for the OAM modes generated by the cascaded HPCFs with the opposite and same helicity were measured from 1545–1590 nm with a step of 5 nm by use of the experimental setup illustrated in Fig. 4 in Ref. [9]. In the experiment, the cascaded HPCFs, i.e., CT + ACT and ACT₁ + ACT₂, were cleaved at the last period of the ACT HPCF to detect the generated OAM modes. As shown in Fig. 4(a), the beam profile and clockwise six-spiral interference pattern, i.e., OAM₋₆ mode, of a single ACT-HPCF exhibited a very low intensity in the core with a wavelength range of 10 nm, i.e., 1570–1580 nm, corresponding to its resonant wavelength 1575 ± 5 nm, as illustrated by the orange borders in Figs. 4(a₁₁) and 4(a₁₂), and the intensity in the core was increased gradually away from the resonant wavelength, where the transmission spectrum is illustrated in Fig. 2(c). It is well-known that the lower intensity in the core of the observed beam profile and interference pattern has, i.e., the higher the coupling efficiency of the resonance dip, the easier it is to

obtain a high-quality OAM mode. As shown in Figs. 4(a₂₁) and 4(a₂₂), the OAM₋₆ mode was also generated by the cascaded CT + ACT HPCFs, while the wavelength range with a very low intensity in the core was broadened to $\Delta\lambda_r = 35$ nm, i.e., 1550.2 – 5 to 1575.0 + 5 nm, corresponding to the initial resonant wavelength, i.e., 1550.2 and 1575.0 nm, of the CT-HPCF and ACT-HPCF, respectively, as illustrated by the green borders in Figs. 4(a₂₁) and 4(a₂₂). Note that the wavelength range of the cascaded HPCFs, i.e., $\Delta\lambda_r$, is given by the equation $\Delta\lambda_r = \Delta\lambda_i + 10$, indicating that the wavelength range, i.e., $\Delta\lambda_r$, to generate a high-quality OAM mode depended on the resonant wavelength interval, i.e., $\Delta\lambda_i$. Then, the beam profile and interference pattern, i.e., OAM₋₆ mode, for a single ACT₂ - HPCF and cascaded ACT₁ + ACT₂ HPCFs were also measured, where the transmission spectrum is illustrated in Fig. 3(c). It is obvious that a wavelength range with a low intensity in the core of the observed beam profiles and interference patterns was broadened from 10 to 35 nm, as illustrated by the green border in Figs. 5(b₂₁) and 5(b₂₂), corresponding to the initial resonant wavelength from 1554.2 – 5–1580.5 + 5 nm. Thus, the wavelength range to generate OAM modes could be tuned by cascading HPCFs with different wavelength intervals. Compared with the ACT₁ + ACT₂ HPCFs, the whole intensity of the CT + ACT HPCFs is stronger than it, indicating that a higher-quality OAM mode could be generated within a broader wavelength range by a compact CT + ACT HPCFs.

The mechanical torsion responses of the cascaded HPCFs with the opposite and same helicity were investigated. The two ends of the cascaded HPCFs were fixed by a fiber rotator and holder, respectively, where the length of the twisted fiber is 100 mm. And the fiber rotator was clockwise or anticlockwise

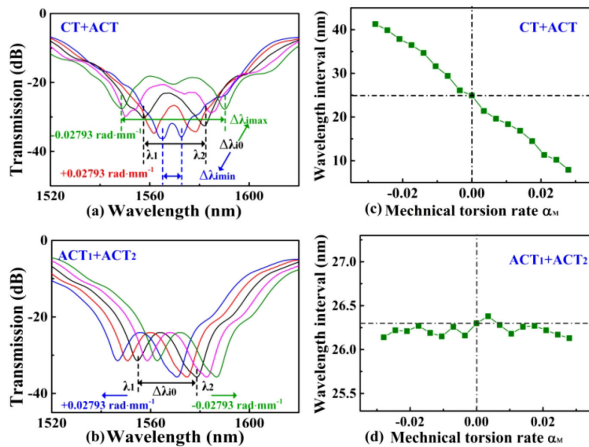


Fig. 5. Transmission spectrum evolution of the cascaded (a) CT + ACT and (b) $ACT_1 + ACT_2$ HPCFs, while the mechanical torsion rate, α_M , varies from $+0.02793$ to -0.02793 rad/mm, and the original spectrum is shown in the black curve; measured resonant wavelength interval of the (c) CT + ACT and (d) $ACT_1 + ACT_2$ HPCFs as a function of the mechanical torsion rate, α_M .

rotated from 0° – 240° with a step of 30° , i.e., the mechanical torsion rate of α_M varies from $+0.02793$ to -0.02793 rad/mm. It is well-known that the helical pitch of the HPCF would be effectively reduced or increased as the mechanical torsion is applied, resulting in a red or blue shift of the resonant wavelength [23]. As shown in Fig. 5(a), the two resonant wavelengths, i.e., λ_1 , λ_2 , of the cascaded CT + ACT HPCFs shifted to a longer and shorter wavelength under the clockwise mechanical torsion, respectively, while the opposite process occurred under the anticlockwise mechanical torsion, resulting in a variation of the resonant wavelength interval, i.e., $\Delta\lambda_i$ [24]. The original spectrum, i.e., $\alpha_M = 0$, was marked in black, where the initial resonant wavelength range, i.e., $\Delta\lambda_{i0} = 24.9$ nm. And the torsion rate of $\alpha_M = \pm 0.02793$ rad/mm resulted in the variation from $\Delta\lambda_{i\min}$ to $\Delta\lambda_{i\max}$, i.e., 7.9–41.3 nm, indicating that the wavelength range, i.e., $\Delta\lambda_r$ to generate the OAM mode is 17.9–51.3 nm. The measured resonant wavelength interval of the cascaded CT + ACT HPCFs as a function of the mechanical torsion rate is illustrated in Fig. 5(c). In addition, the cascaded CT + ACT HPCFs have good repeatability under multiple mechanical torsion tests. However, as shown in Figs. 5(b) and 5(d), the two resonant wavelengths of the cascaded $ACT_1 + ACT_2$ HPCFs exhibited a blue and red shift synchronously under the clockwise and anticlockwise torsion rate, respectively, indicating that the resonant wavelength interval and wavelength range remained the same, i.e., 26.3 and 36.3 nm, respectively. Thus, the wavelength range to generate a high-quality OAM mode of the cascaded CT + ACT HPCFs could be tuned by applying the appropriate mechanical torsion, attributing to the opposite-helicity responses.

In conclusion, we experimentally demonstrated a compact and broad wavelength range tunable OAM mode generator based on cascaded CT + ACT HPCFs. The transmission spectrum of the cascaded HPCFs, i.e., CT + ACT and

$ACT_1 + ACT_2$, is the superposition of two individual HPCFs spectra, regardless of the cascaded helical direction. As for the CT + ACT HPCFs, the wavelength range to generate OAM modes could be broadened not only by cascading HPCFs with different resonant wavelength intervals but also by applying the appropriate mechanical torsion. Hence, our compact and broad wavelength range tunable OAM mode generators could be used in high-capacity optical communications.

Funding. Shenzhen Key Lab of Photonic Devices and Sensing Systems for Internet of Things; National Natural Science Foundation of China (61635007, 61905155); Natural Science Foundation of Guangdong Province (2019A050510047, 2019B1515120042).

Disclosures. The authors declare no conflicts of interest.

REFERENCES

- Z. Xie, S. Gao, T. Lei, S. Feng, Y. Zhang, F. Li, J. Zhang, Z. Li, and X. Yuan, *Photon. Res.* **6**, 743 (2018).
- X. Li, H. Ma, H. Zhang, M. Tang, H. Li, J. Tang, and Y. Wang, *Appl. Phys. Lett.* **114**, 081903 (2019).
- S. Furhapter, A. Jesacher, S. Bernet, and M. Ritsch-Marte, *Opt. Express* **13**, 689 (2005).
- Z. Bai, M. Li, Y. Wang, J. Tang, Z. Zhang, S. Liu, C. Fu, Y. Zhang, J. He, Y. Wang, and C. Liao, *Appl. Phys. Express* **12**, 072004 (2019).
- S. Li, Q. Mo, X. Hu, C. Du, and J. Wang, *Opt. Lett.* **40**, 4376 (2015).
- H. Wu, S. Gao, B. Huang, Y. Feng, X. Huang, W. Liu, and Z. Li, *Opt. Lett.* **42**, 5210 (2017).
- C. Fu, S. Liu, Z. Bai, J. He, C. Liao, Y. Wang, Z. Li, Y. Zhang, K. Yang, B. Yu, and Y. Wang, *J. Lightwave Technol.* **36**, 1683 (2018).
- Y. Zhang, Z. Bai, C. Fu, S. Liu, J. Tang, J. Yu, C. Liao, Y. Wang, J. He, and Y. Wang, *Opt. Lett.* **44**, 61 (2019).
- C. Fu, S. Liu, Y. Wang, Z. Bai, J. He, C. Liao, Y. Zhang, F. Zhang, B. Yu, S. Gao, Z. Li, and Y. Wang, *Opt. Lett.* **43**, 1786 (2018).
- S. Yao, G. Ren, Y. Shen, Y. Jiang, B. Zhu, and S. Jian, *IEEE Photon. Technol. Lett.* **30**, 99 (2018).
- S. Pidshety, S. Pachava, P. Gregg, S. Ramachandran, G. Brambilla, and B. Srinivasan, *Opt. Lett.* **42**, 4347 (2017).
- W. Zhang, L. Huang, K. Wei, P. Li, B. Jiang, D. Mao, F. Gao, T. Mei, G. Zhang, and J. Zhao, *Opt. Lett.* **41**, 5082 (2016).
- Z. Zhao, J. Wang, S. Li, and A. E. Willner, *Opt. Lett.* **38**, 932 (2013).
- N. Zhou, S. Zheng, X. Cao, Y. Zhao, S. Gao, Y. Zhu, M. He, X. Cai, and J. Wang, *Sci. Adv.* **5**, eaau9593 (2019).
- L. Li and X. Zhou, *Sci. Rep.* **8**, 5128 (2018).
- T. Wang, F. Wang, F. Shi, F. Pang, S. Huang, T. Wang, and X. Zeng, *J. Lightwave Technol.* **35**, 2161 (2017).
- F. Xia, Y. Zhao, and H. Hu, *Opt. Laser Technol.* **112**, 436 (2019).
- Y. Guo, Y. Liu, Z. Wang, H. Zhang, B. Mao, W. Huang, and Z. Li, *Opt. Laser Technol.* **118**, 8 (2019).
- Y. Zhao, Z. Liu, Y. Liu, C. Mou, T. Wang, and Y. Yang, *Opt. Lett.* **44**, 5905 (2019).
- C. Fu, Y. Wang, Z. Bai, S. Liu, Y. Zhang, and Z. Li, *Opt. Lett.* **44**, 459 (2019).
- C. Zhu, H. Zhao, and H. Li, *Opt. Commun.* **423**, 81 (2018).
- B. H. Lee and J. Nishii, *Appl. Opt.* **38**, 3450 (1999).
- C. Fu, Y. Wang, S. Liu, Z. Bai, J. Tang, L. Shao, and X. Liu, *Opt. Lett.* **44**, 1984 (2019).
- W. Shin, B.-A. Yu, Y.-C. Noh, J. Lee, and D.-K. Ko, *Opt. Lett.* **32**, 1214 (2007).